The Astrophysical Journal, 779:5 (16pp), 2013 December 10 doi:10.1088/0004-637X/779/1/5
© 2013. The American Astronomical Society. All rights reserved. Printed in the U.S.A.

THERMAL EMISSION OF WASP-14b REVEALED WITH THREE *SPITZER* ECLIPSES

Jasmina Blecic[1], Joseph Harrington[1,2], Nikku Madhusudhan[3], Kevin B. Stevenson[1], Ryan A. Hardy[1], Patricio E. Cubillos[1,2], Matthew Hardin[1], Christopher J. Campo[1], William C. Bowman[1], Sarah Nymeyer[1], Thomas J. Loredo[4], David R. Anderson[5], and Pierre F. L. Maxted[5]
[1] 1Planetary Sciences Group, Department of Physics, University of Central Florida, Orlando, FL 32816-2385, USA
[2] Max-Planck-Institut für Astronomie, D-69117 Heidelberg, Germany
[3] Department of Physics and Department of Astronomy, Yale University, New Haven, CT 06511, USA
[4] Center for Radiophysics and Space Research, Space Sciences Building, Cornell University Ithaca, NY 14853-6801, USA
[5] Astrophysics Group, Keele University, Keele, Staffordshire ST5 5BG, UK; jasmina@physics.ucf.edu
Received 2011 November 6; accepted 2013 September 25; published 2013 November 15

ABSTRACT

Exoplanet WASP-14b is a highly irradiated, transiting hot Jupiter. Joshi et al. calculate an equilibrium temperature ($T_{\rm eq}$) of 1866 K for zero albedo and reemission from the entire planet, a mass of 7.3 ± 0.5 Jupiter masses ($M_{\rm J}$), and a radius of 1.28 ± 0.08 Jupiter radii ($R_{\rm J}$). Its mean density of 4.6 g cm^{-3} is one of the highest known for planets with periods less than three days. We obtained three secondary eclipse light curves with the *Spitzer Space Telescope*. The eclipse depths from the best jointly fit model are 0.224% ± 0.018% at 4.5 μm and 0.181% ± 0.022% at 8.0 μm. The corresponding brightness temperatures are 2212 ± 94 K and 1590 ± 116 K. A slight ambiguity between systematic models suggests a conservative 3.6 μm eclipse depth of 0.19% ± 0.01% and brightness temperature of 2242 ± 55 K. Although extremely irradiated, WASP-14b does not show any distinct evidence of a thermal inversion. In addition, the present data nominally favor models with day–night energy redistribution less than ∼30%. The current data are generally consistent with oxygen-rich as well as carbon-rich compositions, although an oxygen-rich composition provides a marginally better fit. We confirm a significant eccentricity of $e = 0.087 \pm 0.002$ and refine other orbital parameters.

Key words: eclipses – planets and satellites: atmospheres – planets and satellites: individual (WASP-14b) – techniques: photometric

Online-only material: color figures, supplemental data (FITS) file (tar.gz)

1. INTRODUCTION

The *Spitzer Space Telescope* (Werner et al. 2004) is the most widely used facility for measuring thermal properties of extrasolar planets. *Spitzer* systematics are well studied and modeled, providing an invaluable resource for exoplanet characterization (Seager & Deming 2010). This has enabled the measurement of tens of atmospheres, using the detection of primary and secondary eclipses as the most prolific method of investigation to date.

The planet-to-star flux ratio is enhanced in the infrared due to the rising planetary thermal emission and the dropping stellar emission, enabling detection of planetary emission through high-precision photometric measurements. Combining several secondary-eclipse observations measured in broad *Spitzer* bandpasses with the Infrared Array Camera (IRAC; Fazio et al. 2004), a low-resolution dayside spectrum from the planet can be reconstructed, revealing key atmospheric and physical parameters. These measurements can further be used to constrain atmospheric composition, thermal structure, and ultimately the formation and evolution of the observed planet.

WASP-14b represents an intriguing object for such an analysis, having characteristics not so common for close-in, highly irradiated giant planets. Joshi et al. (2009) discovered it as a part of the SuperWASP survey (Wide-Angle Search for Planets; Pollacco et al. 2006; Collier Cameron et al. 2006, 2007). Photometric and radial-velocity observations revealed a planetary mass of 7.3 ± 0.5 $M_{\rm J}$ and a radius of 1.28 ± 0.08 $R_{\rm J}$. Its density ($\rho = 4.6$ g cm^{-3}) is significantly higher than typical hot-Jupiter densities of 0.34–1.34 g cm^{-3} (Loeillet et al. 2008a). The planet is also very close to its star (semi-major axis 0.036 ± 0.001 AU), and has a significant orbital eccentricity, refined slightly to $e = 0.087 \pm 0.002$ in this work.

Detailed spectroscopic analyses of the stellar atmosphere determined that the star belongs to the F5 main-sequence spectral type with a temperature of 6475 ± 100 K and high lithium abundance of log N(Li) = 2.84 ± 0.05. F-type stars with this temperature should have depleted Li, being close to the Li gap or "Boesgaard gap" (Boesgaard & Tripicco 1986; Balachandran 1995). However, the high amount of Li and a relatively high rotational speed of $v \sin(i) = 4.9 \pm 1.0$ km s^{-1} indicate that WASP-14 is a young star. Comparing these results with models by Fortney et al. (2007) for the range of planetary masses and radii led Joshi et al. (2009) to constrain the age of the system to 0.5–1.0 Gyr.

Joshi et al. (2009) also discuss the high eccentricity of the planet. Because WASP-14b has a very small orbital distance, probable scenarios for such a significant eccentricity (their $e = 0.091 \pm 0.003$) would be either that the system age is comparable to the tidal circularization time scale or there is a perturbing body.

Husnoo et al. (2011) performed long-term radial-velocity measurements to discover or reject the presence of a third body. They refined the orbital eccentricity to $e = 0.088 \pm 0.003$. They argue that this planet has undergone some degree of orbital evolution, but that it is still subject to strong tidal forces. They state that since there is no observable unambiguous trend in residuals with time, there is no firm evidence for a planetary companion. This would establish a new lower limit for the semimajor axis at which orbital eccentricity can survive tidal evolution for the age of the system.

Table 1
Observation Information

Channel	Observation Date	Start Time (JD)	Duration (s)	Exposure Time (s)	Number of Frames
Main science observation					
Ch1	2010 Mar 18	2455274.4707	28055.4	2	13760
Ch2	2009 Mar 18	2454908.8139	19998.7	2 × 2	2982
Ch4	2009 Mar 18	2454908.8139	19998.7	12	1481
Pre-observation					
Ch2+4	2009 Mar 18	2454908.7877	2019	2	213
Post-observation					
Ch2+4	2009 Mar 18	2454909.0455	367	2 × 2, 12	10

We obtained three secondary eclipse light curves at 3.6 μm, 4.5 μm, and 8.0 μm using *Spitzer*. We present analytic light-curve models that incorporate corrections for systematic effects that include the new Stevenson et al. (2012a) pixel sensitivity mapping technique, a Keplerian orbital model, estimates of infrared brightness temperatures, and constraints on atmospheric composition and thermal structure.

In Section 2, we describe our observations. Section 3 discusses data reduction procedures. Section 4 presents our photometry and Section 5 discusses the modeling techniques and results from each dataset. Section 6 presents constraints on the orbit of WASP-14b, and Section 7 reveals the atmospheric structure and composition. In Section 8, we discuss our results and in Section 9 we present our conclusions. Data files containing the light curves, best-fit models, centering data, photometry, etc., are included as electronic supplements to this article.

2. OBSERVATIONS

The *Spitzer* IRAC instrument observed two events: one at 3.6 μm in 2010 March (Knutson's program 60021, Warm *Spitzer*) and one observation simultaneously in two wavelength bands (4.5 and 8.0 μm) in 2009 March (Harrington's program 50517, *Spitzer* cryogenic mission). The observation at 3.6 μm (channel 1) was made in subarray mode with 2 s exposures, while the observations at 4.5 and 8.0 μm (channels 2 and 4) were made in stellar mode (2×2,12) with pairs of 2 s frames taken in the 4.5 μm band for each 12 s frame in the 8.0 μm band. This mode was used to avoid saturation in channel 2.

We have pre- and post-observation calibration frames for the 4.5 and 8.0 μm observation. Prior to the main observation, we exposed the array to a relatively bright source (see Section 5.2). That quickly saturated charge traps in the detector material, reducing the systematic sensitivity increase during the main observation. Post-eclipse frames of blank sky permit a check for warm pixels in the aperture. The *Spitzer* pipeline version used for the 3.6 μm observation is S.18.14.0 and for the 4.8 and 8.0 μm observation is S18.7.0. The start date of each observation, duration, exposure time and total number of frames are given in Table 1.

3. DATA REDUCTION

3.1. Background

Our analysis pipeline is called Photometry for Orbits, Eclipses, and Transits (POET). It produces light curves from *Spitzer* Basic Calibrated Data (BCD) frames, fits models to the light curves, and assesses uncertainties. The derived parameters constrain separate orbital and atmospheric models. In this section, we give a general overview of POET. Subsequent sections will provide details as needed.

Each analysis starts by identifying and flagging bad pixels in addition to the ones determined by the *Spitzer* bad pixel mask (see Section 4). Then we perform centering. Due to the ∼0.1% relative flux level of secondary-eclipse observations and *Spitzer's* relative photometric accuracy of 2% (Fazio et al. 2004), we apply a variety of centering routines, looking for the most consistent. We test three methods to determine the point-spread function (PSF) center precisely: center of light, two-dimensional Gaussian fitting, and least asymmetry (see Supplementary Information of Stevenson et al. 2010 and Lust et al. 2013). The routines used for each data set are given below. We then apply 5×-interpolated aperture photometry (Harrington et al. 2007), where each image is re-sampled using bilinear interpolation. This allows the inclusion of partial pixels, thus reducing pixelation noise (Stevenson et al. 2012a). We subtract the mean background within an annulus centered on the star and discard frames with bad pixels in the photometry aperture.

Spitzer IRAC has two main systematics, which depend on time and the sub-pixel position of the center of the star. To find the best time-dependent model (the "ramp"), we fit a variety of systematic models from the literature, and some of our own, using a Levenberg–Marquardt χ^2 minimizer (Levenberg 1944; Marquardt 1963). We use our newly developed (Stevenson et al. 2012a) BiLinearly Interpolated Subpixel Sensitivity (BLISS) mapping technique to model intrapixel sensitivity variation (see Section 3.2). The BLISS method can resolve structures inaccessible to the widely used two-dimensional polynomial fit (Knutson et al. 2008; Machalek et al. 2009; Fressin et al. 2010). It is faster and more accurate than the mapping technique developed by Ballard et al. (2010), which uses a Gaussian-weighted interpolation scheme and is not feasibly iterated in each step of Markov-Chain Monte Carlo (MCMC; see next section for details on modeling systematics).

To determine the best aperture size, we seek the smallest standard deviation of normalized residuals (SDNR) among different aperture sizes for the same systematic model components. The best ramp model at that aperture size is then determined by applying the Bayesian (BIC) and Akaike (AIC) information criteria (Liddle 2007), which compare models with different numbers of free parameters (see Section 3.3). The BIC and AIC cannot be used to compare BLISS maps with differing grid resolutions, or BLISS versus polynomial maps (see Section 3.2), but BLISS has its own method for optimizing its grid (Stevenson et al. 2012a).

To explore the parameter space and to estimate uncertainties, we use an MCMC routine (see Section 3.3). We model the systematics and the eclipse event simultaneously, running four independent chains until the Gelman & Rubin (1992) convergence test for all free parameters drops below 1%. Our MCMC routine can model events separately or simultaneously, sharing parameters such as the eclipse midpoint, ingress/egress times, or duration.

Finally, we report mid-times in both BJD_{UTC} (Barycentric Julian Date, BJD, in Coordinated Universal Time) and BJD_{TT} (BJD_{TDB}, Barycentric Dynamical Time), calculated using the Jet Propulsion Laboratory (JPL) Horizons system, to facilitate handling discontinuities due to leap seconds and to allow easy comparison of eclipse mid-times (see Eastman et al. 2010 for discussion of timing issues).

3.2. Modeling Systematics

Modeling systematics is critical to recovering the extremely weak signal of an exoplanetary atmosphere against the stellar and/or background noise, particularly when using instrumentation not specifically built for the job. Several re-analyses of early *Spitzer* eclipse data sets underscore this. For example, our group's initial analysis of an HD 149026b lightcurve Harrington et al. (2007) found two χ^2 minima, with the deeper eclipse having the deeper minimum. This analysis used the bootstrap Monte Carlo technique as described without statistical justification and too simplistically by Press et al. (1992). The re-analysis by Knutson et al. (2009b), using MCMC, preferred the lower value, which additional observations confirmed. Our own re-analysis, by Stevenson et al. 2012a, agreed with Knutson et al. Another example is the Désert et al. (2009) re-analysis of the putative detection of H_2O on HD 189733b by Tinetti et al. (2007). Désert et al. found a shallower transit that did not support the detection. Although the number of such discrepancies in the *Spitzer* eclipse and transit literature is not large compared to the many dozens of such measurements, they serve as cautionary tales. It is critical to use only the most robust statistical treatments (e.g., MCMC rather than bootstrap), to compare dozens of systematic models using objective criteria (like BIC), and to worry about minutiae like the differences between various centering and photometry methods. Re-analyses of photometric work done with such care have uniformly been in agreement. Most of these appear as notes in original papers stating that another team confirmed the analysis (e.g., Stevenson et al. 2012b).

Spitzer's IRAC channels can exhibit both time-dependent and position-dependent sensitivity variations. These variations can be up to ∼3%, much more than typical (0.01%–0.5%) eclipse depths. The 3.6 and 4.5 μm bands use InSb detectors, and the 5.8 and 8.0 μm bands use Si:As detectors. Although each type of systematic is strongest in a different set of channels, many authors reported both systematics in both sets of channels (Stevenson et al. 2010; Reach et al. 2005; Charbonneau et al. 2005; Campo et al. 2011), so we test for them all in each observation.

The time-varying sensitivity ("ramp") is most pronounced at 8.0 μm (Charbonneau et al. 2005; Harrington et al. 2007) and is very weak, often nonexistent, in the InSb channels. It manifests as an apparent increase in flux with time, and at 8.0 μm it is attributed to charge trapping. Observing a bright (>250 MJy sr^{-1} in channel 4), diffuse source ("preflashing") saturates the charge traps and produces a flatter ramp (Knutson et al. 2009b). An eclipse is easily separated from the ramp by fitting, but not without adding uncertainty to the eclipse depth. Model choice is particularly important for weak eclipses, where a poor choice can produce an incorrect eclipse depth. To model the ramp effect, we test over 15 different forms of exponential, logarithmic, and polynomial models (see Stevenson et al. 2012a, Equations (2)–(11)).

InSb detectors can have intrapixel quantum efficiency variations, which strongly affects *Spitzer's* underresolved PSF and requires accurate (∼0.01-pixel) determination of the stellar center location. This intrapixel sensitivity is greatest at pixel center and declines toward the edges by up to 3.5% (Morales-Calderón et al. 2006). It is also not symmetric about the center and the amplitude of the effect varies from pixel to pixel. Over the total duration of the observation, the position varies by several tenths of a pixel. Since the stellar center oscillates over this range frequently, this systematic is adequately sampled during a single eclipse observation. Observing with fixed pointing minimizes the effect (Reach et al. 2005; Charbonneau et al. 2005; Harrington et al. 2007; Stevenson et al. 2010).

Our BLISS method (Stevenson et al. 2012a) maps a pixel's sensitivity on a fine grid of typically over 1000 "knots" within the range of stellar centers. It then uses bilinear interpolation to calculate the sensitivity adjustment for each observation from the nearest knot values ($M(x, y)$ in Equation (1)). To compute the map, we divide the observed fluxes by the eclipse and ramp models, and assume that any residual fluxes are related to the stellar center's position in the pixel (hence the need for accurate stellar centering; see above). We average the residuals near each knot to calculate its value. Each data point contributes to one knot, and each knot comes from a small, discontiguous subset of the data. The map is recalculated after each MCMC iteration and is used to calculate χ^2 in the next iteration. The MCMC does not directly vary the knot values, but the values change slightly at each iteration. This method quickly converges.

The crucial setup item in BLISS is determining the knot spacing (i.e., bin size or resolution). The bin size must be small enough to catch any small-scale variation, but also large enough to ensure no correlation with the eclipse fit (see Section 5.1). Either bilinear (BLI) or nearest-neighbor (NNI) interpolation can generate the sensitivities from the knots. Assuming accurate centering, BLI should always outperform NNI. The bin size where NNI outperforms BLI thus indicates the centering precision and determines the bin size for that particular data set. If NNI always outperforms BLI, that indicates very weak intrapixel variability, and intrapixel modeling is unnecessary.

Compared to polynomial intrapixel models, the SDNR improves with BLISS mapping, but this would be expected of any model with more degrees of freedom. Previously, we have used BIC and AIC to evaluate whether a better fit justifies more free parameters. Both BIC and AIC are approximations to the Bayes factor, which is often impractical to calculate. Both criteria apply a penalty to χ^2 for each additional free parameter (k, in Equations (2) and (3)), allowing comparison of model goodness-of-fit to the same dataset for different models. However, both criteria assume that every data point contributes to each free parameter. That is, they assume that changing any data point potentially changes *all* of the free parameters, as do all other information criteria we have researched. However, each BLISS knot value comes from only a specific, tiny fraction of the data. Changing any individual data point changes exactly one BLISS knot. Thus, the knots each count for much less than one free parameter in the sense of the assumptions of BIC and AIC, but not zero (i.e., they each increment k by much less than one). Because BLISS violates their assumptions, BIC and AIC are inappropriate for comparing models using BLISS to models that do not use it. It is still possible to compare two models using BLISS maps with the same knot grid because the increment in the penalty terms would be the same for both grids and would thus not affect the comparison. See Appendix A of Stevenson et al. (2012a) for a more statistically rigorous discussion.

At this point in BLISS's development, we are still working on an appropriate comparison metric. What we do know is that BLISS resolves fine detail in pixel sensitivity that, in many cases, is not compatible with any low-order polynomial form. For example, Stevenson et al. (2012a) show (and compensate for) the effects of pixelation in digital aperture photometry, and demonstrate how our interpolated aperture photometry reduces pixelation bias. For this paper, the eclipse-depth values are similar between BLISS and non-BLISS analyses, and the

residuals are smaller with BLISS, since it is taking out some of these effects in a way that low-order polynomial models cannot (see Figure 5 and examples in Stevenson et al. 2010). We have a large excess of degrees of freedom, so we adopt the BLISS results. We continue to use BIC for ramp-model selection.

3.3. Modeling Light Curves and the Best Fit Criteria

To find the best model, for each aperture size we systematically explore every combination of ramp model and intrapixel sensitivity model. The final light curve model is

$$F(x, y, t) = F_s R(t) M(x, y) E(t), \quad (1)$$

where $F(x, y, t)$ is the aperture photometry flux, F_s is the constant system flux outside of the eclipse, $R(t)$ is the time-dependent ramp model, $M(x, y)$ is the position-dependent intrapixel model, and $E(t)$ is the eclipse model (Mandel & Agol 2002). We fit each model with a Levenberg–Marquardt χ^2 minimizer and calculate SDNR, BIC, and AIC (note that parameter uncertainties, and hence MCMC, are not needed for these calculations).

To estimate uncertainties, we use our MCMC routine with the Metropolis–Hastings random walk algorithm, running at least 10^6 iterations to ensure accuracy of the result. This routine simultaneously fits eclipse parameters and *Spitzer* systematics. It explores the parameter phase space, from which we determine uncertainties fully accounting for correlations between the parameters. The depth, duration, midpoint, system flux, and ramp parameters are free. Additionally, the routine can model multiple events at once, sharing the eclipse duration, midpoint, and ingress/egress times. These joint fits are particularly appropriate for channels observed together (see Campo et al. 2011 for more details about our MCMC routine).

To avoid fixing any model parameter during MCMC, we use Bayesian priors (e.g., Gelman 2002). This is particularly relevant for noisy or low signal-to-noise ratio (S/N) datasets where some parameters like ingress and egress times are not well constrained by the observations. For them we use informative priors taken from the literature (see Section 5 for the values used in this analysis).

Photometric uncertainties used in our analyses are derived by fitting an initial model with a Levenberg–Marquardt χ^2 minimizer and re-scaling it so reduced $\chi^2 = 1$. This is needed because *Spitzer* pipeline uncertainties have often been overestimated (Harrington et al. 2007), sometimes by a factor of two or three. Along with the BCD frames, the Spitzer Science Center provides images giving the uncertainties of the BCD pixels. The calculations behind these images include uncertainty in the absolute flux calibration, which effect we divide out. The *Spitzer*-provided errors are thus too large for exoplanet eclipses and transits, but they do contain information about the relative noisiness of different pixels.

Most workers ignore the uncertainty frames and calculate a single per-frame uncertainty from their root mean square (rms) model residuals, sometimes taken over just a short time span. This has the effect of fixing the reduced chi-squared to 1, and possibly ignoring red noise, depending on the time span of residuals considered. We do use the *Spitzer*-provided uncertainties, resulting in slightly differing uncertainties per frame. However, this approach can produce reduced chi-squared values of 0.3, and sometimes 0.1, as the *Spitzer* uncertainties are computed with absolute calibration in mind. So, we also re-scale the per-frame uncertainties to give a reduced chi-squared of 1. As a practical matter, the variation in our uncertainties is a few percent and the typical uncertainty is the same as with the rms method applied to the entire dataset, which accounts for a global average of red noise.

Rescaling the uncertainties is changing the dataset, and BIC can only compare different models applied to a single dataset. So, we use just one rescaling per aperture size, and fit all the models to that dataset. This works because the reasonable models for a given dataset all produce nearly the same scaling factor. The rank ordering of models is not altered by the scaling factor. In Section 5.4, we lists the rescaling factor for each dataset.

After deriving new uncertainties, we re-run the minimizer and then run MCMC. If MCMC finds a lower χ^2 than the minimizer, we re-run the minimizer starting from the MCMC's best value. The minimizer will find an even better χ^2. We then restart the MCMC from the new minimizer solution. We ensure that all parameters in four independent MCMC chains converge within 1% according to the Gelman & Rubin (1992) test. We also inspect trace plots for each parameter, parameter histograms, and correlation plots for all parameter pairs.

Our measures of goodness of fit are SDNR, BIC, and AIC values (Liddle 2007):

$$\mathrm{BIC} = \chi^2 + k \ln N, \quad (2)$$

$$\mathrm{AIC} = \chi^2 + 2k, \quad (3)$$

where k is the number of free parameters, and N is the number of data points. These criteria penalize additional free parameters in the system, with better fits having lower values. To appropriately compare BIC or AIC values for a given aperture size, and determine the best fit, we use the same uncertainties for each dataset, and model all combinations of ramp models and intrapixel model. SDNR values are used to compare different aperture sizes using the same model. The lowest value defines the best aperture size.

Equally important is the correlation in the residuals (see Section 5.1). We plot and compare the scaling of binned model residuals versus bin size (Pont et al. 2006; Winn et al. 2008) with the theoretical $1/\sqrt{N}$ scaling for the rms of Gaussian residuals. A significant deviation between those two curves indicates time-correlated variation in the residuals and possible underestimation of uncertainties if only their point-to-point variation is considered. Note that our uncertainty estimation uses the residuals' global rms, so we already account for a global average of correlated noise.

After MCMC is finished, we study parameter histograms and pairwise correlations plots, as additional indicators of good posterior exploration and convergence.

4. WASP-14b PHOTOMETRY

For our analyses, we used BCD frames generated in the *Spitzer* IRAC pipeline (Fazio et al. 2004). The pipeline version used for each observation is given in Section 2. Our data reduction procedure started with applying *Spitzer*'s bad pixel masks and with our procedure for flagging additional bad pixels (Harrington et al. 2007). In each group of 64 frames and at each pixel position, we applied two-iteration outlier rejection, which calculated the frame median and the standard deviation from the median (not mean), and flagged pixels that deviated by more than 4σ. Then we found the stellar centroid for the

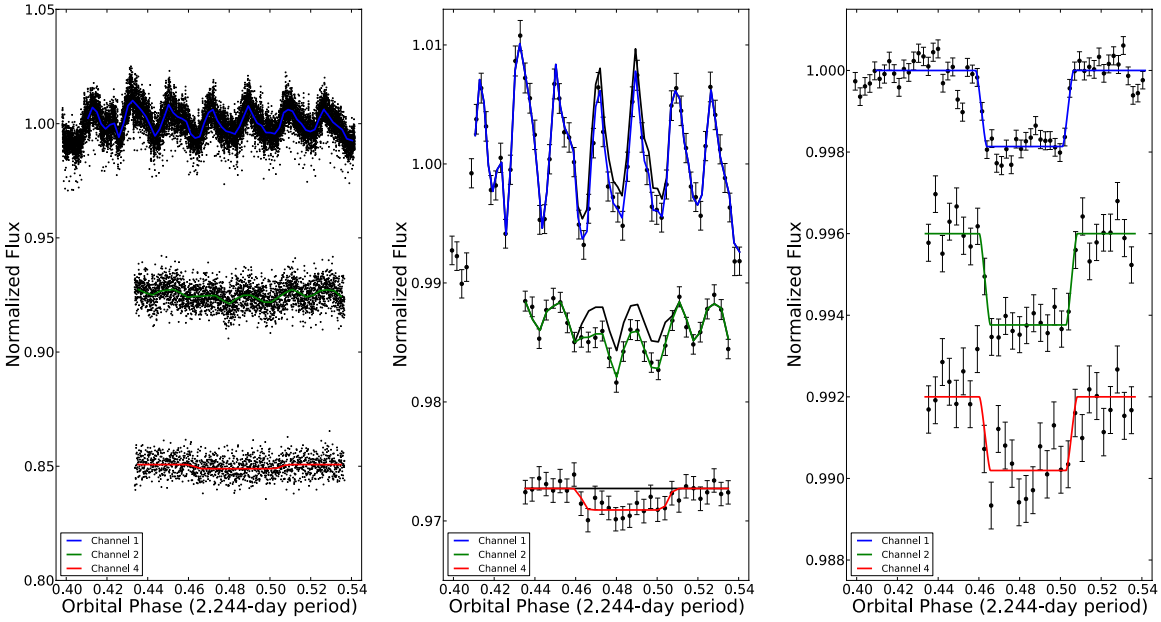

Figure 1. Raw (left), binned (center, 60 points per bin), and systematics-corrected (right) secondary-eclipse light curves of WASP-14b at 3.6, 4.5, and 8.0 μm. The results are normalized to the system flux and shifted vertically for clarity. The colored lines are best-fit models and the error bars are 1σ uncertainties. The black lines in the binned plots are models without an eclipse. As seen in the same plots of channels 2 and 4, a ramp model is not needed to correct for the time-dependent systematic even without clipping any initial data points. The channel 1 model omits early data due to an initial pointing drift (see Section 5.1).

(A color version of this figure is available in the online journal.)

photometry by using a two-dimensional Gaussian fit to data in an aperture radius of four pixels.

After subtracting the mean background (annuli given in Section 5.4), light curves were extracted using 5×-interpolated aperture photometry (Harrington et al. 2007) for every aperture radius from 2.25 to 4.25 pixels in 0.25 pixel steps.

To calculate the BJD of each exposure, we used the mid-exposure time of each frame, based on the UTCS-OBS value in the FITS header and the frame number. We performed our barycentric light-time correction using our own code and the coordinates of the *Spitzer* spacecraft from the Horizons ephemeris system of the JPL. The times are corrected to BJD_{TDB} to remove the effects of leap seconds and light-travel time across the exoplanet's orbit.

5. WASP-14b SECONDARY ECLIPSES

Here, we discuss each channel's analysis and model selection in detail, particularly focusing on channel 1, due to the demanding analysis of that data set. In Subsection 5.1, we give our control plots, as an example of how we verify that our results are indeed the best solution for the particular data set. We present each channel separately, followed by a joint fit to all data. Figure 1 shows our best-fit eclipse light curves. Figure 2 shows how the rms of the residuals scales with bin size, a test of correlated noise. In Table 11 in the Appendix, we summarize parameters for the WASP-14 system as derived from this analysis and found in the literature.

5.1. Channel 1–3.6 μm

The channel-1 observation lasted 7.8 hr, giving ample baseline before and after the secondary eclipse. The telescope drifted at the start of the observation. Models with initial data points removed produce better fits with lower values for SDNR. We therefore ignored some initial data (∼36 minutes, 1100 of 13760 points). Figure 3 compares SDNR values for models with different ramps and with and without exclusion of the initial data.

Starting from an aperture radius of 2.25 pixels and continuing in increments of 0.25 pixels, we tested all of the ramp models (linear, rising, exponential, sinusoidal, double exponential, logarithmic, etc.). Corresponding equations are listed in Stevenson et al. (2012a). To determine the best solution, we consider our best-fit criteria (see Section 3.3) and study the correlation plots. Most of the models produced obvious bad fits, so minimizer and shorter MCMC runs eliminated them. The best aperture radius is 2.75 pixels (see Figure 3, bottom panel). We tested the dependence of eclipse depth on aperture radius (Anderson et al. 2010). The trend in some events may indicate a slightly imperfect background removal (see Figure 4). The effect is less than 1σ on the eclipse depth.

Figure 5 presents the channel-1 BLISS map and Figure 6 gives the correlation coefficients between the knot values and the eclipse depth. As stated in the Section 3.2, the most important variable to consider with BLISS is the bin size, which defines the resolution in position space. The position precision for channel 1, measured as the rms of the position difference on consecutive frames, is significantly different for the x and y axes (see Figure 7). We considered a range of bin sizes for both BLI and NNI around the calculated precision. The best bin size for this data set, determined when NNI outperformed BLI, is 0.004 pixels for x and 0.01 for y.

We also tested two-dimensional polynomial intrapixel models (Knutson et al. 2008; Stevenson et al. 2010; Campo et al. 2011):

$$V_{IP}(x, y) = p_1 y^2 + p_2 x^2 + p_3 xy + p_4 y + p_5 x + 1, \quad (4)$$

where x and y are relative to the pixel center nearest the median position and p_1–p_5 are free parameters. As noted in Section 3.2, we currently lack a quantitative model-selection criterion between polynomial and BLISS intrapixel models, but BIC can apply within a group of BLISS models with the

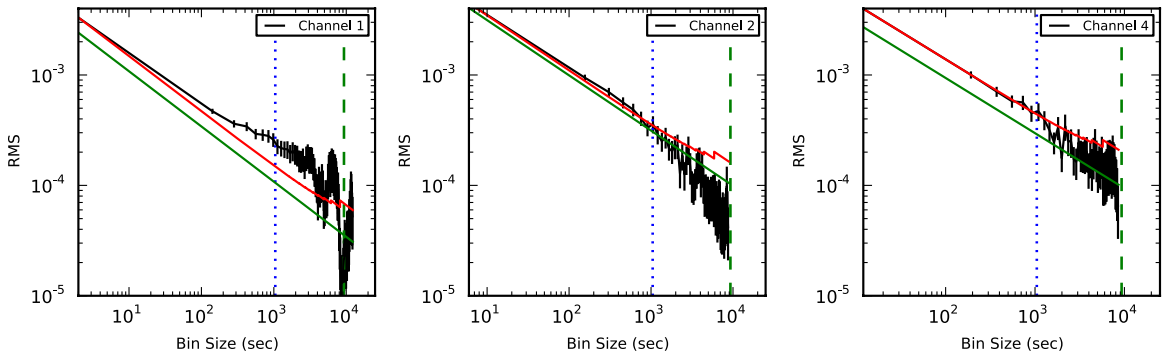

Figure 2. Correlations of the residuals for the three secondary eclipse light curves of WASP-14b, following Pont et al. (2006). The black line represents the rms residual flux versus bin size. The red line shows the predicted standard error scaling for Gaussian noise. The green line shows the Poisson-noise limit. The black vertical lines at each bin size depict 1σ uncertainties on the rms residuals, $\mathrm{rms}/\sqrt{2N}$, where N is the number of bins (see Jeffreys 1961, Section 3.41 and Sivia & Skilling 2006, Section 3.3 for a derivation including the factor of two, which arises because this is the uncertainty scaling of the rms, not the mean). The dotted vertical blue line indicates the ingress/egress timescale, and the dashed vertical green line indicates the eclipse duration timescale. Large excesses of several σ above the red line would indicate correlated noise at that bin size. Inclusion of 1σ uncertainties shows no noise correlation between the ingress/egress and eclipse duration timescales anywhere except for channel 1 ingress/egress, which hints 3σ at a correlation (adjacent points on this plot are themselves correlated). Since the relevant timescale for eclipse depths is the duration timescale, we do not scale the uncertainties. See Section 5.1.1 for further discussion.

(A color version of this figure is available in the online journal.)

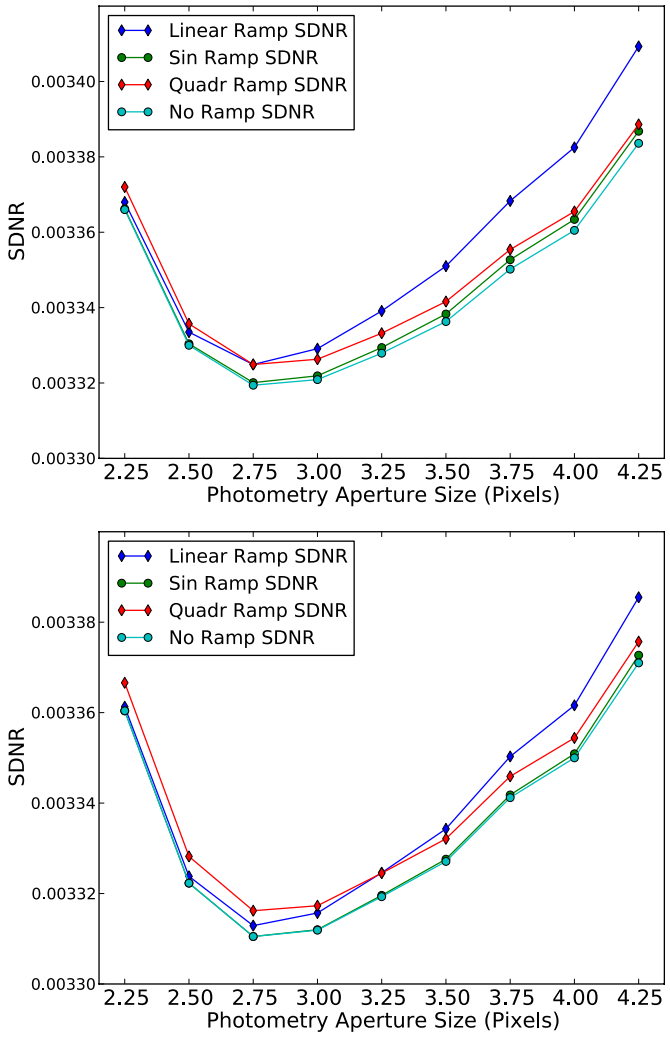

Figure 3. SDNR versus aperture size for different ramp models in channel 1. A lower value indicates a better model fit. Top: all observational points included (*no-preclip*). Bottom: same, but with 1100 initial points excluded (*preclip*).

(A color version of this figure is available in the online journal.)

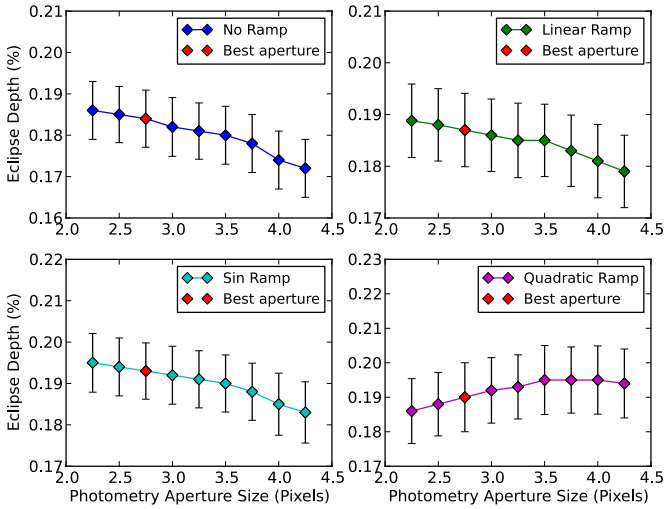

Figure 4. Best-fit eclipse depths as a function of photometry aperture size for channel 1. The four best ramp models are plotted (see below). The red point indicates the best aperture size for that channel. The eclipse-depth uncertainties are the result of 10^5 MCMC iterations. The trend shows insignificant dependence of eclipse depth on aperture size (less than 1σ).

(A color version of this figure is available in the online journal.)

Table 2
Comparison BLISS and Best Polynomial Model

Ramp Model	BLISS		Polynomial-Quadratic	
	SDNR	BIC	SDNR	BIC
No ramp	0.003313	12350.0	0.0033853	12593.2
Linear	0.003311	12342.3	0.0033852	12588.5
Sinusoidal	0.003316	12342.2	0.0033855	12590.5
Quadratic	0.003310	12351.5	0.0033850	12597.3

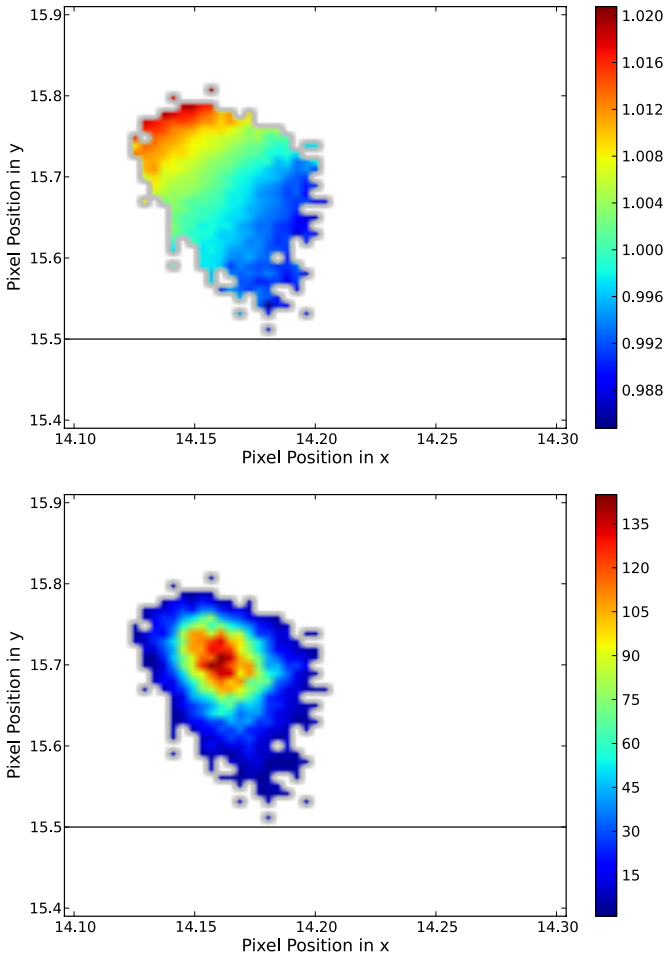

Figure 5. Top: BiLinearly Interpolated Subpixel Sensitivity (BLISS) map of channel 1. Redder (bluer) colors indicate higher (lower) subpixel sensitivity. The horizontal black line defines the lower pixel boundary. Bottom: Pointing histogram. Colors indicate the number of points in a given bin.

(A color version of this figure is available in the online journal.)

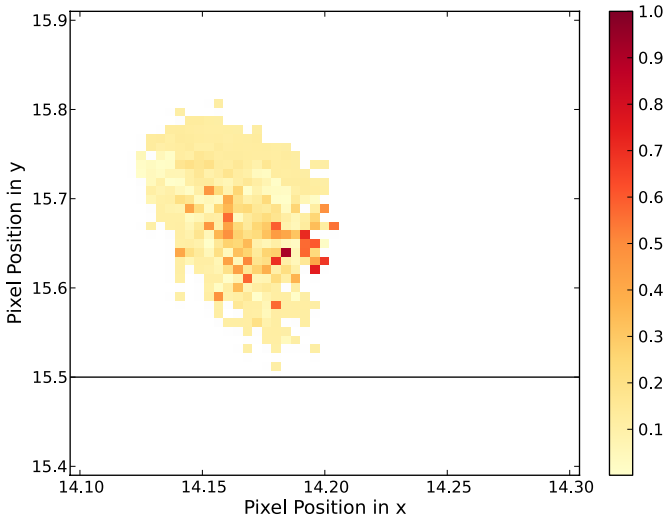

Figure 6. Correlation coefficients between eclipse depth and computed BLISS map knots for channel 1. The correlation regions (in red) indicate that it is necessary to compute the BLISS map at each MCMC step, to assess the uncertainty on the eclipse depth correctly.

(A color version of this figure is available in the online journal.)

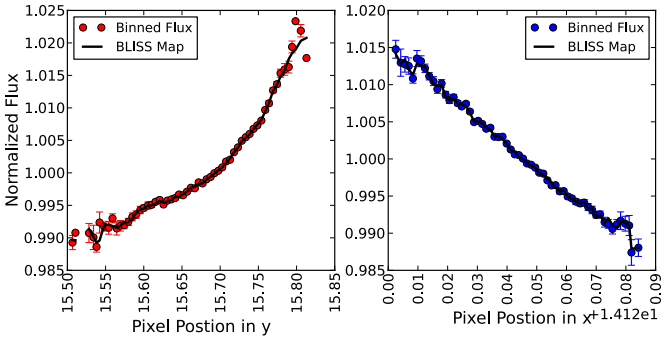

Figure 7. BLISS map and data of channel 1 integrated along the x (right) and y (left) axes. BLISS effectively fits the position-dependent sensitivity variation.

(A color version of this figure is available in the online journal.)

Table 3
Channel 1 Ramp Models

Ramp Model	SDNR	BIC	Eclipse Depth (%)
No ramp	0.0033129	12350.0	0.184 ± 0.007
Linear	0.0033105	12342.3	0.187 ± 0.007
Sinusoidal	0.0033162	12342.2	0.193 ± 0.007
Quadratic	0.0033105	12351.5	0.190 ± 0.010

same grid. BLISS reduces SDNR significantly compared to polynomial models (see Table 2), but so would many models with more free parameters. We use BLISS because it can handle variations that polynomials cannot follow. See Stevenson et al. (2012a) for other tests that compare polynomial and BLISS intrapixel models.

To determine the uncertainties in the model parameters, we explored the posterior probability distribution of the model given the data with MCMC. We used a Bayesian informative prior for the secondary-eclipse ingress and egress time ($t_{2-1} = 1046.8 \pm 43.9$ s), calculated from unpublished WASP photometric and radial-velocity data. All other parameters (eclipse midpoint, eclipse duration, eclipse depth, system flux, and ramp parameters) were left free.

Considering all the above criteria (see also Section 3.3), we selected four ramp models (see Table 3). The first is without a ramp model, while the other three are

$$R(t) = 1 + r_0\,(t - 0.5), \tag{5}$$

$$R(t) = 1 + a\,\sin(2\pi(t - t_1)) + b\,\cos(2\pi(t - t_2)), \tag{6}$$

$$R(t) = 1 + r_1\,(t - 0.5) + r_2\,(t - 0.5)^2, \tag{7}$$

where t is orbital phase and a, b, r_0, r_1, and r_2 are free parameters.

The models produce almost identical SDNR values. However, upon studying the BIC values and the inconsistent trend in the eclipse depths between models with similar BIC values (see Table 3), we concluded that there is no single best ramp model for this data set.

Therefore, we again use Bayes's theorem and the BIC approximation to the Bayes factor to compare two different models to the data. Following Raftery (1995) Equations (7) and (8), we calculate the posterior odds, i.e., to which extent the data support one model over the other:

$$\text{Posterior Odds} = \text{Bayes Factor } x \text{ Prior Odds}, \tag{8}$$

Table 4
Bayes Factor for Model 2 against Model 1

Ramp Model	BIC	ΔBIC	B_{21}	$1/B_{21}$
No ramp	12350.0	7.8	0.02	49.4
Linear	12342.3	0.1	0.95	1.05
Sinusoidal	12342.2	0.0	...	...
Quadratic	12351.5	9.3	0.009	104.6

$$\frac{P(M_2 \mid D)}{P(M_1 \mid D)} = \frac{P(D \mid M_2)}{P(D \mid M_1)} \frac{P(M_2)}{P(M_1)}, \quad (9)$$

where M_1 and M_2 denote two models, and D denotes the data. $P(M_1 \mid D)$ and $P(M_2 \mid D)$ denote the posterior distributions of the models given the data, $P(D \mid M_1)$ and $P(D \mid M_2)$ denote the marginal probabilities of the data given the model, and $P(M_1)$ and $P(M_2)$ denote the prior probabilities of the models.

The first term on the right side of Equation (9) is the Bayes factor for model 2 against model 1, which we will denote as B_{21}. If $B_{21} > 1$, the data favor model 2 over model 1, and vice versa.

Raftery (1995, see his Equations (20)–(22)) further derives an approximation to the Bayes factor, using BIC, that defines the ratio of marginal probabilities for the two models as

$$B_{21} = \frac{P(D \mid M_2)}{P(D \mid M_1)} \approx e^{-\Delta \mathrm{BIC}/2}, \quad (10)$$

where $\Delta \mathrm{BIC} = \mathrm{BIC}(M_2) - \mathrm{BIC}(M_1)$. We calculate this quantity for each of our ramp models.

Table 4 gives the probability ratio, or the Bayes factor, for each of our ramp models compared to the model with the smallest BIC value (the sinusoidal model, see Table 3). These models are all within the 3σ confidence interval of the best model, indicating an ambiguous situation. In the atmospheric modeling below, we use the eclipse depth and uncertainty from each of the two extreme models (no-ramp and sinusoidal), and show that the resulting atmospheric models are consistent with each other. A representative single eclipse depth and uncertainty that spans the two points from the joint fit model (see Section 5.4) is $0.19\% \pm 0.01\%$, and the corresponding brightness temperature is 2242 ± 55 K.

5.1.1. On WASP-14 Activity

In this channel, we detect time correlation of noise at the 3σ level on time scales of $<10^3$ s and $\lesssim 2\sigma$ up to about the 3000 s scale (Figure 2, left panel, and Figure 8). The longest time scale with even a 2σ detection of correlation is about 1/7 the eclipse duration, so we do not expect a major effect on the planetary results. Although not perfect, our ramp and intrapixel models typically remove instrumental effects (e.g., see the middle and right panels of Figure 2), raising the question of stellar activity.

One would not expect a hot mid-F star (with a small convective zone) like WASP-14 to be active or to show much spot activity even if it were a moderate rotator. Nonetheless, we analyzed the WASP light curve of WASP-14 to determine whether it shows periodic modulation due to the combination of magnetic activity and stellar rotation. The stellar rotation values derived by Joshi et al. (2009) together with the estimated stellar radius imply a rotation period of about 12 days or more, assuming that the rotation axis of the star is approximately aligned with the orbital axis of the planet. We used the sine-wave fitting method described by Maxted et al. (2011) to calculate a

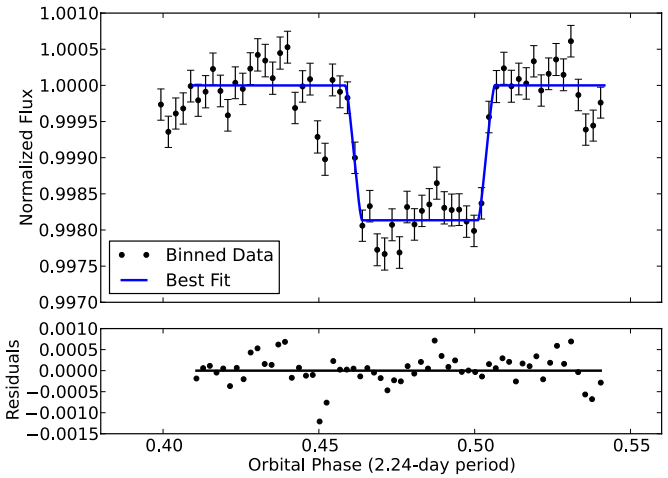

Figure 8. Residuals for the channel 1 observations (lower panel) display some level of correlated noise both in and out of the eclipse.
(A color version of this figure is available in the online journal.)

periodogram over 4096 uniformly spaced frequencies from 0 to 1.5 cycles day^{-1}. The false-alarm probability (FAP) for the strongest peak in these periodograms was calculated using a bootstrap Monte Carlo method also described by Maxted et al. (2011).

We did not find any significant periodic signals (FAP < 0.05) in the WASP data, apart from frequencies near 1 cycle day^{-1}, which are due to instrumental effects. We examined the distribution of amplitudes for the most significant frequency in each Monte Carlo trial and used these results to estimate a 95% upper confidence limit of 1 milli-magnitude (0.1%) for the amplitude of any periodic signal in the lightcurve.

In our work on dozens of *Spitzer* eclipses, we have often found the same channel to behave differently at different times, even on the same star. Our systematics removal algorithms correct the worst effects, which are consistent, but there is sometimes still some significant baseline scatter or oscillation. While one might expect certain kinds of stars to be relatively stable, *Spitzer* can reach $\sigma \sim 0.01\%$ eclipse-depth sensitivity, and non-periodic stellar oscillations of this scale and at these wavelengths are not well studied. So, it is not fully clear whether these effects come from the observatory or the star.

Since scatter and oscillation often persist during an eclipse (when the planet is behind the star), and since a change in planetary signal of the magnitude seen would generally mean an implausibly dramatic change in the planet, we feel justified in treating the scatter or oscillation phenomenologically. In this case, our per-point uncertainties account for a global average of correlated noise. MCMC accounts for any correlation between eclipse and model parameters, and the rms versus bin size analysis, now including error bars, determined that the time correlation was not significant near the time scale of interest (Figure 2). Also, a larger uncertainty was assigned to the eclipse depth based on model ambiguity (above), which provides an additional margin of safety.

5.2. Channel 2–4.5 μm

Channel 2 and 4 were observed at the same time. We first modeled each channel separately, determining the best aperture size, time-variability (ramp) model, and bin size for BLISS. Then we applied a joint fit. For both channels 2 and 4, we again used the Bayesian informative prior for the values of ingress

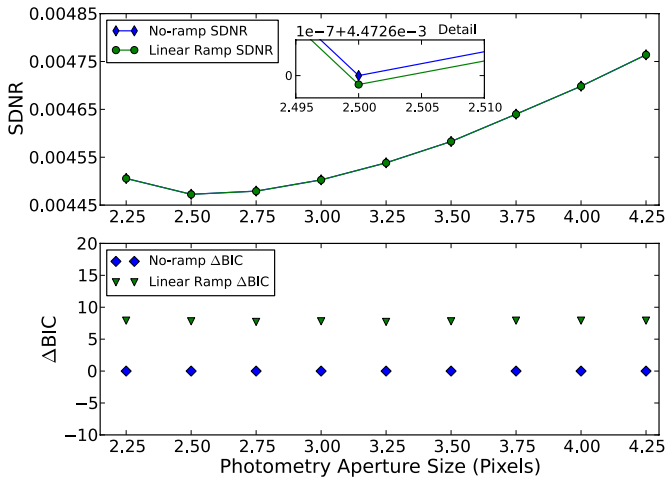

Figure 9. Channel 2 comparison between linear and no ramp models. The plots show the SDNR and ΔBIC versus aperture size. A lower value indicates a better model fit.

(A color version of this figure is available in the online journal.)

Table 5
Channel 2 Ramp Models

Ramp Model	SDNR	BIC	Eclipse Depth (%)
No Ramp	0.0044726	2964.2	0.224 ± 0.012
Linear	0.0044725	2971.9	0.224 ± 0.018
Quadratic	0.0044723	2979.9	0.241 ± 0.025
Rising	0.0044726	2980.1	0.224 ± 0.021
Lin+Log	0.0044690	2983.9	0.228 ± 0.017

and egress times ($t_{2-1} = 1046.8 \pm 43.9$ s), calculated from unpublished WASP photometric and radial-velocity data. All other parameters were left free.

The observation in channel 2 lasted 5.5 hr. There was no stabilization period observed in the data, so no initial points were removed from the analysis.

Following the criteria in Section 3.1, we tested each of our ramp models (Table 5) at each of the aperture radii from 2.25–4.25 pixels in 0.25 pixel increments. Figure 9 shows SDNR and ΔBIC versus aperture size for our two best ramp models. We note insignificantly different SDNR values between the two ramp models, which suggests that the best dataset (aperture radius of 2.50) does not depend on the model being fit. The BIC favors the no-ramp model. The no-ramp model is 47 times more probable than the linear model.

We also tested the dependence of eclipse depth on aperture radius (see Figure 10). The eclipse depths are well within 1σ.

Prior to the science observations in channels 2 and 4, we observed a 212-frame preflash (see Section 2) on a diffuse, uniformly bright H II emission region centered at $\alpha = 10, 45, 02.2$, $\delta = -59, 41, 10.1$. The portion of the array within the aperture of the science observation in each channel was uniformly illuminated. For channel 2, the average flux within the 2.5 pixel aperture is ∼200 MJy sr^{-1}, while for the 3.5 pixel aperture of channel 4 it is ∼1800 MJy sr^{-1}.

As expected, channel 2 shows no increase in flux during the preflash observation (see Figure 11, left panel) nor during the main science observation (see Figure 1, raw data). The preflash observation in channel 4 saturated within the 30 minutes, eliminating the ramp effect in channel 4.

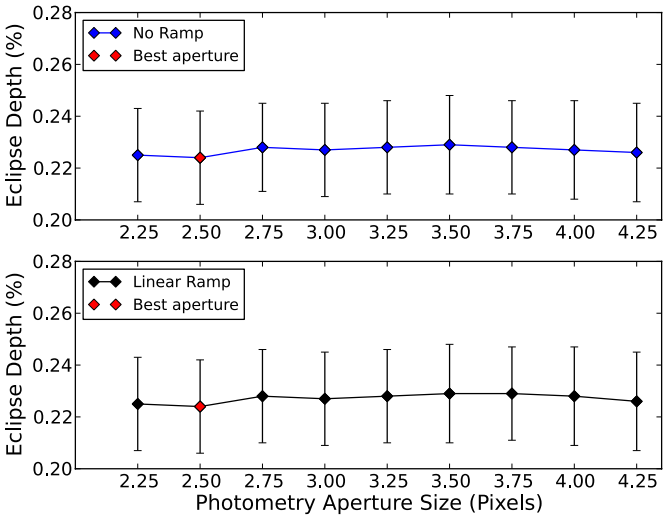

Figure 10. Best-fit eclipse depths as a function of photometry aperture size for channel 2. The red point indicates the best aperture size for that channel. The eclipse-depth uncertainties are the result of 10^5 MCMC iterations. The trend shows insignificant dependence of eclipse depth on aperture size (much less than 1σ).

(A color version of this figure is available in the online journal.)

Table 6
Channel 4 Ramp Models

Ramp Model	SDNR	BIC	Eclipse Depth (%)
No ramp	0.0039799	1459.2	0.181 ± 0.013
Linear	0.0039770	1464.3	0.182 ± 0.012
Rising	0.0039799	1466.4	0.198 ± 0.030
Quadratic	0.0039763	1471.3	0.181 ± 0.018
Lin+Log	0.0039799	1481.0	0.181 ± 0.024

Regardless of the preflash observations, we tested the full set of ramp equations and discarded obvious bad fits after shorter runs. Among acceptable fits, the lowest BIC value (see Table 5) determined that there is no significant ramp effect in the channel 2 dataset.

Each observation ended with a 10-frame, post-eclipse observation of blank sky in the same array position as the science observations to check for warm pixels in the photometric aperture. There were none.

To remove intrapixel variability we again apply our new BLISS technique, and also Equation (4). As with channel 1, the projection plot shows BLISS following significant variations that the polynomial does not fit well. The position precisions in channel 2 are 0.02 pixels for x and 0.014 pixels for y. The best bin sizes are 0.028 pixels in x and 0.023 pixels in y. The best aperture size, ramp model, and BLISS bin sizes are then used in our joint fit, which gave us the eclipse depths and the brightness temperatures in Section 5.4.

5.3. Channel 4–8.0 μm

Again, no stabilization period was observed in the 8.0 μm dataset data set, hence no initial data points were removed. The preflash eliminated the ramp entirely, according to BIC (Table 6).

Figure 12 plots the SDNR and ΔBIC values versus aperture size at 8.0 μm. For our two best ramp models (Table 6) the smallest SDNR value is at 3.50 pixels (which determined our best aperture size), and the lowest BIC value at that aperture

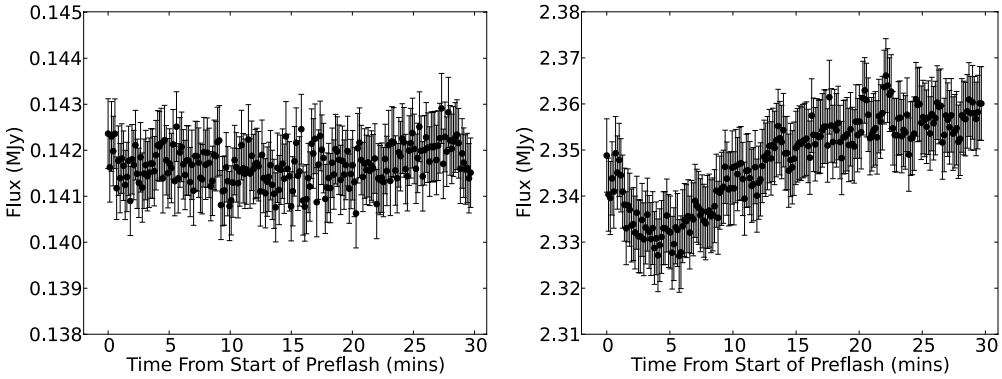

Figure 11. Preflash light curves for channel 2 (left) and channel 4 (right). The plots show binned data over 30 minutes of observation. The preflash source is a bright H II emission region. Without a preflash, the science observations would show a similar or possibly longer ramp in channel 4.

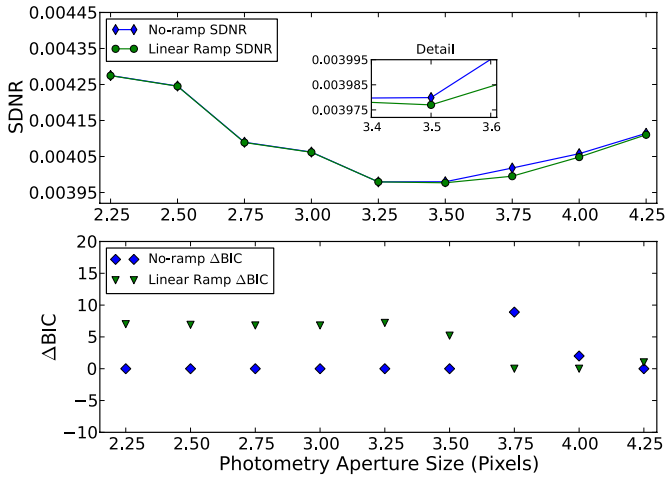

Figure 12. Channel 4 comparison between linear and no-ramp models. The plots show SDNR and ΔBIC versus aperture size. A lower value indicates a better model fit.

(A color version of this figure is available in the online journal.)

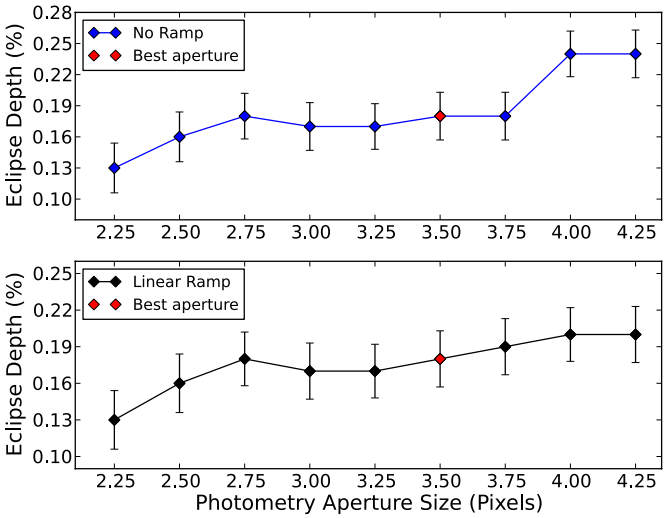

Figure 13. Best-fit eclipse depths as a function of photometry aperture size for channel 4. The red point indicates the best aperture size for that channel. The eclipse-depth uncertainties are the result of 10^5 MCMC iterations. This channel has the lowest S/N (∼8). The aperture size of 2.25 pixels shows excess noise. Excluding it, the trend exhibits insignificant dependence of eclipse depth on aperture size (less than 1σ).

(A color version of this figure is available in the online journal.)

size is for the model without a ramp. We again test for the dependence of eclipse depth on aperture size (Figure 13).

Even though intrapixel variability is not so strong in channels 3 and 4, pixelation can be significant at any wavelength if the aperture is small (see Stevenson et al. 2012a and Anderson et al. 2011). This justifies testing whether BLISS can give a better fit. Upon testing a full set of bin sizes, we concluded that NNI always outperforms BLI, indicating that variability from pixelation is insignificant.

5.4. Joint Fit

Our final models fit all data simultaneously. The models shared a common eclipse duration for channels 1, 2, and 4 and a common midpoint time for channels 2 and 4, which were observed together. We used the same priors as above. The Gelman & Rubin (1992) convergence diagnostic dropped below 1% for all free parameters after 50,000 iterations. Histograms for some interesting parameters for channel 1 appear on the left side of Figure 14. The middle plots show the pairwise correlations (marginal distributions) of these parameters. The histograms on the right are for the joint fit of channels 2 and 4. All other histograms are similarly Gaussian, confirming that the phase space minimum is global and defining the parameter uncertainties. Tables 7 and 8 report two joint-fit results for our two best ramp models in channel 1 (linear and sinusoidal), along with photometric results and modeling choices from the individual fits. Light-curve files including the best-fit models, centering data, photometry, etc., are included as electronic supplements to this article.

6. ORBIT

We fit the midpoint times from the *Spitzer* lightcurves simultaneously with the available radial velocity curves and transit photometry in order to provide updated estimates of system orbital parameters. The timing of secondary eclipse is a strong constraint on the shape and orientation of the orbit. The two eclipses for the linear and sinusoidal joint fit (Tables 7 and 8) have an insignificant difference in phases (less than 0.5σ), and the linear joint fit has slightly lower BIC value. Hence, we picked the linear joint fit phases for the use in the orbital analysis. The two eclipses occur at phases 0.4825 ± 0.0003 and 0.4841 ± 0.0005 (using the Joshi et al. 2009 ephemeris), with a weighted mean after a 37 s eclipse-transit light-time correction of 0.48273 ± 0.00025, indicating that $e \cos \omega = -0.0271 \pm 0.0004$. The phases differ from each other by approximately 3σ, but depend strongly on the accuracy of the ephemeris used to compute them.

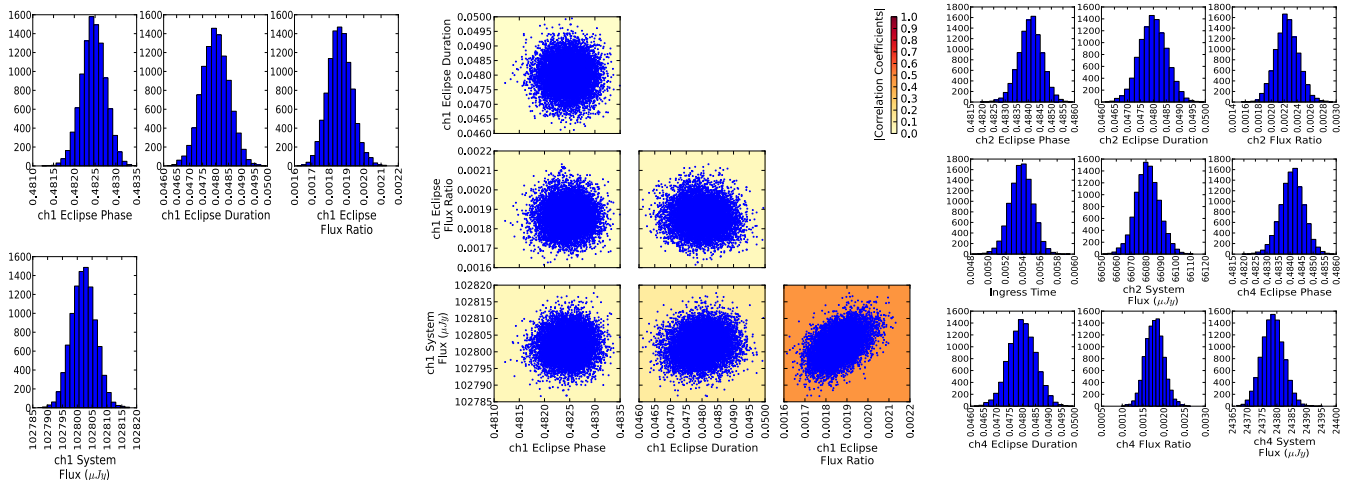

Figure 14. Left and center: sample parameter histograms and parameter correlations for channel 1. The background color depicts the absolute value of the correlation coefficient. Right: sample parameter histograms for channel 2 and channel 4, produced in the joint fit. All other parameter histograms are similarly Gaussian. Every 10th step in the MCMC chain is used to decorrelate consecutive values.

(A color version of this figure is available in the online journal.)

Table 7
Joint Best-fit Eclipse Light-curve Parameters (Channel 1–Linear Ramp)

Parameter	Channel 1	Channel 2	Channel 4
Array position ($\bar{x}$, pixel)	14.16	23.82	24.6
Array position ($\bar{y}$, pixel)	15.69	24.11	21.9
Position consistency[a] (δ_x, pixel)	0.005	0.02	0.021
Position consistency[a] (δ_y, pixel)	0.012	0.014	0.025
Aperture size (pixel)	2.75	2.5	3.5
Sky annulus inner radius (pixel)	8.0	12.0	12.0
Sky annulus outer radius (pixel)	20.0	30.0	30.0
System flux F_s (Jy)	102802 ± 4	66083 ± 7	24381 ± 3
Eclipse depth (%)	0.187 ± 0.007	0.224 ± 0.018	0.181 ± 0.022
Brightness temperature (K)	2225 ± 39	2212 ± 94	1590 ± 116
Eclipse midpoint (orbits)	0.4825 ± 0.0003	0.4842 ± 0.0005	0.4842 ± 0.0005
Eclipse midpoint (BJD_{UTC} −2,450,000)	5274.6609 ± 0.0006	4908.9290 ± 0.0011	4908.9290 ± 0.0011
Eclipse midpoint (BJD_{TDB} −2,450,000)	5274.6617 ± 0.0006	4908.9298 ± 0.0011	4908.9298 ± 0.0011
Eclipse duration (t_{4-1}, hr)	2.59 ± 0.03	2.59 ± 0.03	2.59 ± 0.03
Ingress/egress time (t_{2-1}, hr)	0.290 ± 0.007	0.290 ± 0.007	0.290 ± 0.007
Ramp name	linear	...	...
Ramp, linear term (r_0)	0.0044 ± 0.0010	...	...
Intrapixel method	BLISS	BLISS	...
BLISS bin size in x (pixel)	0.004	0.028	...
BLISS bin size in y (pixel)	0.01	0.023	...
Minimum number of points per bin	4	5	...
Total frames	13693	2972	1432
Rejected frames (%)	0.49	0.34	3.89
Free parameters	6	3	2
AIC value	16695.8	16695.8	16695.8
BIC value	16780.7	16780.7	16780.7
SDNR	0.003311	0.004473	0.003980
Uncertainty scaling factor	0.031968	0.294486	0.342520
Photon-limited S/N (%)	72.7	90.4	68.1

Note. [a] rms frame-to-frame position difference.

We fit a Keplerian orbit model to our secondary eclipse times along with radial velocity data from Husnoo et al. (2011) and Joshi et al. (2009), and transit timing data from both amateur observers and WASP-14b's discovery paper (Joshi et al. 2009). The entire data set comprised 38 RV points, six of which were removed due to the Rossiter–McLaughlin effect, 30 transits, and two eclipses (see Table 9). All times were adjusted to BJD_{TDB} (Eastman et al. 2010). The errors were estimated using our MCMC routine. This fit gave $e = 0.087 \pm 0.002$ and $\omega = 107.^{\circ}1 \pm 0.^{\circ}5$. We did not adjust for any anomalous eccentricity signal from the stellar tidal bulge as described by Arras et al. (2012) because the predicted amplitude of this effect is smaller than the uncertainty on the eccentricity, and much smaller than the eccentricity itself. With our new data, we refine the ephemeris to $T_{BJD_{TDB}} = 2454827.06666(24)+2.2437661(11)\,N$, where T is the time of transit and N is the number of orbits

Table 8
Joint Best-fit Eclipse Light-curve Parameters (Channel 1–Sinusoidal Ramp)

Parameter	Channel 1	Channel 2	Channel 4
Array position ($\bar{x}$, pixel)	14.16	23.82	24.6
Array position ($\bar{y}$, pixel)	15.69	24.11	21.9
Position consistency[a] (δ_x, pixel)	0.005	0.02	0.021
Position consistency[a] (δ_y, pixel)	0.012	0.014	0.025
Aperture size (pixel)	2.75	2.5	3.5
Sky annulus inner radius (pixel)	8.0	12.0	12.0
Sky annulus outer radius (pixel)	20.0	30.0	30.0
System flux F_s (Jy)	102616 ± 7	66083 ± 7	24381 ± 3
Eclipse depth (%)	0.193 ± 0.007	0.224 ± 0.017	0.181 ± 0.021
Brightness temperature (K)	2258 ± 38	2212 ± 89	1590 ± 111
Eclipse midpoint (orbits)	0.4825 ± 0.0003	0.4843 ± 0.0005	0.4843 ± 0.0005
Eclipse midpoint (BJD_{UTC} −2,450,000)	5274.6609 ± 0.0006	4908.9291 ± 0.0011	4908.9291 ± 0.0011
Eclipse midpoint (BJD_{TDB} −2,450,000)	5274.6617 ± 0.0006	4908.9298 ± 0.0011	4908.9298 ± 0.0011
Eclipse duration (t_{4-1}, hr)	2.59 ± 0.03	2.59 ± 0.03	2.59 ± 0.03
Ingress/egress time (t_{2-1}, hr)	0.290 ± 0.007	0.290 ± 0.007	0.290 ± 0.007
Ramp name	sinusoidal	...	...
Ramp, cosine phase offset (t_2)	0.5356 ± 0.0016	...	...
Intrapixel method	BLISS	BLISS	...
BLISS bin size in x (pixel)	0.004	0.028	...
BLISS bin size in y (pixel)	0.01	0.023	...
Minimum number of points per bin	4	5	...
Total frames	13693	2972	1432
Rejected frames (%)	0.49	0.34	3.89
Free parameters	6	3	2
AIC value	16695.9	16695.9	16695.9
BIC value	16780.8	16780.8	16780.8
SDNR	0.003316	0.004473	0.003980
Uncertainty scaling factor	0.031968	0.294485	0.342520
Photon-limited S/N (%)	72.6	90.4	68.1

Note. [a] rms frame-to-frame position difference.

elapsed since the transit time (see Table 10). We find that the new ephemeris reduces the difference between the two eclipse phases to less than 1.6σ. Performing an ephemeris fit to the transit and eclipse data separately shows that the transit and eclipse periods differ by $(1.1 \pm 0.8) \times 10^{-5}$ days, a 1.5σ result that limits apsidal motion, $\dot{\omega}$, to less than $0.^{\circ}0024$ day^{-1} at the 3σ level (Giménez & Bastero 1995).

The results confirm an eccentric orbit for WASP-14b and improve knowledge of other orbital parameters.

7. ATMOSPHERE

We explore the model parameter space in search of the best-fitting models for a given data set. The model parameterization is described by Madhusudhan & Seager (2009, 2010); Madhusudhan (2012). The sources of opacity in the model include molecular absorption due to H_2O, CO, CH_4, CO_2, TiO, and VO, and collision-induced absorption (CIA) due to H_2–H_2. Our molecular line lists are obtained from Freedman et al. (2008), R. S. Freedman (2009, private communication), Rothman et al. (2005), Karkoschka & Tomasko (2010), and E. Karkoschka (2011, private communication). Our CIA opacities are obtained from Borysow et al. (1997) and Borysow (2002). We explore the model parameter space using a MCMC scheme, as described by Madhusudhan & Seager (2010). However, since the number of model parameters ($n = 10$) exceed the number of data points ($N_{data} = 3$), our goal is not to find a unique fit to the data but, primarily, to identify regions of model phase space that the data exclude. In order to compute the model planet-star flux ratios to match with the data, we divide the planetary spectrum by a Kurucz model of the stellar spectrum derived from Castelli & Kurucz (2004). Our models allow constraints on the temperature structure, molecular mixing ratios, and a joint constraint on the albedo and day–night redistribution.

We find that strong constraints can be placed on the presence of a thermal inversion in WASP-14b even with our current small set of observations. At an irradiation of 3×10^9 erg s^{-1} cm^{-2}, WASP-14b falls in the class of extremely irradiated planets that are predicted to host thermal inversions according to the TiO/VO hypothesis of Fortney et al. (2008). However, the present observations do not show any distinct evidence of a thermal inversion in the dayside atmosphere of WASP-14b. We explored the model parameter space by running $\sim 10^6$ models with and without thermal inversions, using an MCMC scheme as discussed above. We found that the data could not be explained by a thermal inversion model for any chemical composition. On the other hand, the data are easily fit by models with no thermal inversions. While the brightness temperatures in the 3.6 and 4.5 μm channels are consistent with a blackbody spectrum of the planet at $T \sim 2200$ K, the 8 μm flux deviates substantially from the assumption of a blackbody with a brightness temperature of 1668 ± 125 K. In the presence of a thermal inversion, the flux in the 8 μm channel is expected to be much higher than the fluxes in the 3.6 and 4.5 μm channels due to emission features of water vapor and, if present, methane. The low flux observed at 8 μm, therefore, implies strong water vapor and/or methane in absorption, implying the lack of a significant temperature inversion (see Madhusudhan & Seager 2010 for a discussion on inferring thermal inversions). We also note that as mentioned in Section 5.1, the observations yield different planet–star flux

Table 9
Transit Timing Data

Mid-transit Time (BJD_{TDB})	Uncertainty	Source[a]
2455695.4082	0.0012	V. Slesarenkno, E. Sokov[b]
2455668.4790	0.0011	František Lomoz
2455652.7744	0.0014	Stan Shadick, C. Shiels[c]
2455650.5307	0.0018	Lubos Brát
2455650.52789	0.00076	Martin Vrašt'ák
2455650.52566	0.00067	Jaroslav Trnka[d]
2455632.5807	0.0011	E. Sokov, K. N. Naumov[b]
2455318.45101	0.00085	Anthony Ayiomamitis
2455302.7464	0.0010	Stan Shadick[c]
2455264.6021	0.0012	Hana Kučáková[e]
2455264.6017	0.0013	Radek Kocián[f]
2455219.7290	0.0012	Lubos Brát
2454979.643	0.003	Wiggins, AXA
2454968.426	0.001	Srdoc, AXA
2454950.4831	0.0021	Jesionkiewicz, AXA
2454950.4746	0.0014	Lubos Brát
2454950.4745	0.0018	Hana Kučáková[e]
2454950.4731	0.0021	Pavel Marek
2454950.4728	0.0014	Wardak, AXA
2454943.7427	0.0006	Dvorak, AXA
2454941.49799	0.00081	Jaroslav Trnka[d]
2454941.4916	0.0019	František Lomoz
2454934.765	0.001	Brucy Gary, AXA
2454932.5246	0.0014	Radek Dřevěný
2454932.5232	0.0011	Lubos Brát
2454932.5222	0.0013	Jaroslav Trnka[d]
2454932.5219	0.0015	T. Hynek, K. Onderková
2454914.5753	0.0008	Naves, AXA
2454887.6457	0.0014	Georgio, AXA

Notes.
[a] The Amateur Exoplanet Archive (AXA), http://brucegary.net/AXA/x.htm, and Transiting ExoplanetS and Candidates group (TRESCA), http://var2.astro.cz/EN/tresca/index.php, supply their data to the Exoplanet Transit Database (ETD), http://var2.astro.cz/ETD/, which performs the uniform transit analysis described by Poddaný et al. (2010). The ETD Web site provided the AXA and TRESCA numbers in this table, which were converted to BJD_{TDB}.
[b] Sokov E., Naumov K., Slesarenko V. et al., Pulkovo Observatory of RAS, Saint-Petersburg, Russia.
[c] Physics and Engineering Physics Department, University of Saskatchewan, Saskatoon, Saskatchewan, Canada, S7N 5E2.
[d] Municipal Observatory in Slany Czech Republic.
[e] Project Eridanus, Observatory and Planetarium of Johann Palisa in Ostrava.
[f] Kocián R., Johann Palisa, Observatory and Planetarium, Technical University Ostrava, 17. Listopadu 15, CZ-708 33 Ostrava, Czech Republic.

Table 10
Eccentric Orbital Model

Parameter	Value
$e \sin \omega$[a]	0.0831 ± 0.0021
$e \cos \omega$[a]	-0.02557 ± 0.00038
e	0.087 ± 0.002
ω (°)	-107.1 ± 0.5
P (days)[a]	2.2437661 ± 0.0000011
T_0 [a,b]	$2454827.06666 \pm 0.00024$
K (m s^{-1})[a,c]	990 ± 3
γ (m s^{-1})[a,d]	-4987.9 ± 1.6
χ^2	162

Notes.
[a] Free parameter in MCMC fit.
[b] BJD_{TDB}.
[c] Radial velocity semi-amplitude.
[d] Radial velocity offset.

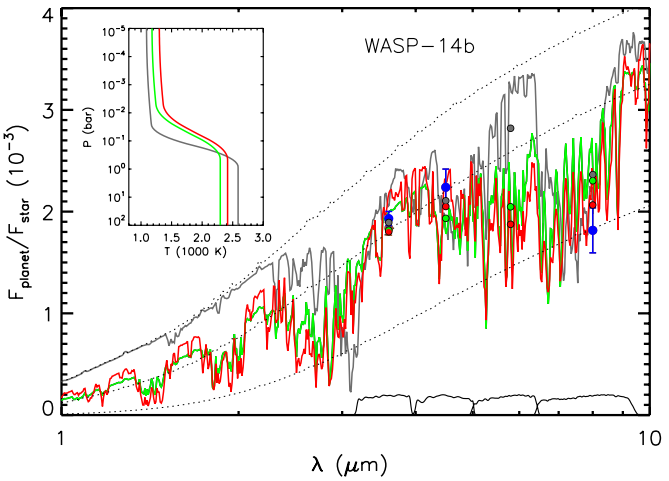

Figure 15. Observations and model spectra for dayside emission from WASP-14b. The blue filled circles with error bars show our observations in *Spitzer* channel 1 (3.6 μm), 2 (4.5 μm), and 4 (8.0 μm). For the 3.6 μm channel, two values are shown, in blue and brown, corresponding to different ramp models used in deriving the eclipse depths (see Section 5.1). The green, red, and gray curves show model spectra with different chemical compositions and without thermal inversions that explain the data; the corresponding pressure–temperature (P–T) profiles are shown in the inset. The green model has molecular abundances in thermochemical equilibrium assuming solar elemental abundances. The red model has 10 times lower CO and 6 times higher H_2O compared to solar abundance chemistry, i.e., more oxygen-rich than solar abundances. The gray model has a carbon-rich chemistry (C/O = 1). The green, red, and gray circles show the model spectra integrated in the *Spitzer* IRAC bandpasses. The oxygen-rich (red) model provides a marginally better fit to the data than the solar and carbon-rich models. The black dotted lines show three blackbody planet spectra at 1600 K, 2200 K, and 2600 K.
(A color version of this figure is available in the online journal.)

contrasts in the 3.6 μm channel for different choices of ramp models. However, as shown in Figure 15, the two extreme values are still consistent at the 1σ level, and as such, lead to similar model conclusions.

We modeled the dayside atmosphere of WASP-14b using the exoplanetary atmospheric modeling method developed by Madhusudhan & Seager (2009, 2010). We use a one-dimensional line-by-line radiative transfer code to model the planetary atmosphere under the assumption of local thermodynamic equilibrium, hydrostatic equilibrium, and global energy balance at the top of the atmosphere. The latter condition assumes that the integrated emergent planetary flux balances the integrated incident stellar flux, accounting for the Bond albedo (A_B) and possible redistribution of energy onto the night side. Our model uses parameterized prescriptions to retrieve the temperature structure and chemical composition from the observations, as opposed to assuming radiative and chemical equilibrium with fixed elemental abundances (Burrows et al. 2008; Fortney et al. 2008).

We find that the data can be explained by models with a wide range of chemical compositions. Figure 15 shows three model spectra with different chemistries, along with the observations: (1) a solar-abundance model (in green in Figure 15) with chemical composition in thermochemical equilibrium assuming solar abundances (TE_{solar}), (2) an oxygen-rich model (in red) with 10× lower CO and 8× higher H_2O, and (3) a carbon-rich model (in gray, e.g., Madhusudhan et al. 2011a, Madhusudhan 2012). The oxygen-rich model fits the data marginally better than the solar abundance model. A slightly lower CO is favored because of the slightly higher 4.5 μm flux compared to the 3.6 μm flux, which means lower absorption due to CO. Higher

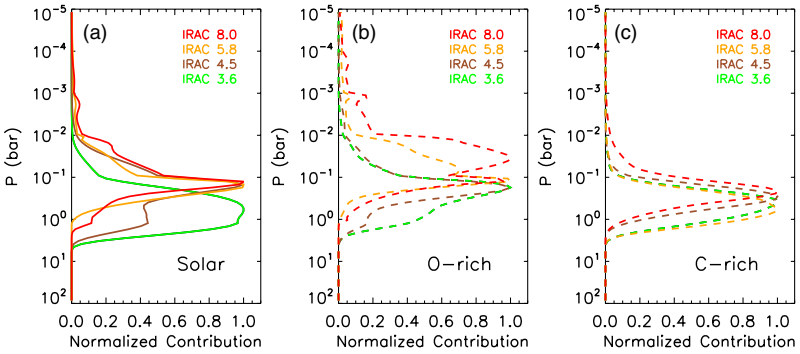

Figure 16. Left: contribution functions in the four *Spitzer* channels corresponding to the green model shown in Figure 15. The legend shows the channel center wavelength in m and the curves are color-coded by the channel. All the contribution functions are normalized to unity. Middle: contribution functions corresponding to the red model shown in Figure 15. Right: contribution functions corresponding to the gray model shown in Figure 15.

(A color version of this figure is available in the online journal.)

absorption due to H_2O is favored by the low 8 μm point. In principle, a lower CO and a higher H_2O, compared to TE_{solar} values, are both possible by having a C/O ratio less than the solar value of 0.54. However, more data would be required to confirm the low CO requirement, because a blackbody of ~2200 K fits the 3.6 and 4.5 μm points just as well.

Models with high C/O ratios (C/O $\geqslant$ 1, i.e., carbon-rich) can lead to strong CH_4, C_2H_2, and HCN absorption in the 3.6 μm and 8 μm channels (e.g., Madhusudhan et al. 2011a, 2011b; Madhusudhan 2012), instead of H_2O absorption in the low-C/O models. As shown in Figure 15, the C-rich model fits the data as well as the solar-abundance model, but less precisely than the model with low C/O (i.e., enhanced H_2O and low CO). Although the data marginally favor an oxygen-rich composition in the dayside atmosphere of WASP-14b, new observations are required to provide more stringent constraints on the C/O ratio. Future observations in the near-infrared, from ground and space, can place further constraints on the temperature structure and composition, especially the C/O ratio, of the dayside atmosphere of WASP-14b. In particular, as shown in Figure 15, near-infrared observations in the 1–2.5 μm range probe spectral features of several oxygen- and carbon-bearing molecules such as H_2O, CO, and CH_4, mixing ratios of which can provide stringent constraints on the C/O ratio (Madhusudhan et al. 2011b). For example, the oxygen-rich models predict deep absorption features in the H_2O bands, contrary to the carbon-rich model, which contains no significant water absorption. *Hubble Space Telescope* WFC3 observations in the 1.1–1.7 μm range can test for water absorption. Furthermore, the models with different C/O ratios also predict different continuum fluxes, which can be observed from ground in the *J*, *H*, and *K* bands (see Madhusudhan 2012).

The models explaining the observations require relatively low day-night energy redistribution in WASP-14b. As shown by the contribution functions in Figure 16, the 3.6 μm IRAC channel probes the atmosphere between 0.1 and 1 bar. Consequently, the high brightness temperature in the 3.6 μm channel indicates a hot planetary photosphere. Over the entire model population explored by our retrieval method, we find that the data allow for up to ~30% of the energy incident on the dayside to be redistributed to the night side (i.e., for zero Bond albedo). For the particular best-fitting model (in red) shown in Figure 15, this fraction is ~25%. For non-zero albedos the fraction is even lower; since the quantity we constrain is $\eta = (1 - A_B)(1 - f_r)$, where A_B is the Bond albedo and f_r is the fraction of the dayside incident energy redistributed to the nightside Madhusudhan & Seager (2009). However, the present constraints on the day-night redistribution are only suggestive and new observations are essential to further constrain the energy redistribution in WASP-14b. For example, observations in atmospheric windows at lower wavelengths, e.g., between 1 and 2 μm, where the black-body of the planetary photosphere would peak, would be critical to further constrain the lower atmospheric thermal structure, and hence the energy budget of the planet's dayside atmosphere. More importantly, phase-curve observations are required to constrain the day-night energy redistribution directly (e.g., Knutson et al. 2007, 2009a).

8. DISCUSSION

The absence of a thermal inversion in the dayside atmosphere of WASP-14b constrains inversion-causing phenomena in irradiated atmospheres. The canonical argument for such inversions is via absorption in the optical by gaseous TiO and VO (Hubeny et al. 2003; Fortney et al. 2008). On the other hand, Spiegel et al. (2009) showed that the high mean molecular masses of TiO and VO would lead to significant gravitational settling of these molecules, thereby depleting them from the upper atmospheres, unless strong vertical mixing keeps them aloft. Additionally, the abundances of inversion-causing molecules might also be influenced by stellar activity and photochemistry (Knutson et al. 2010). Consequently, the real cause of thermal inversions in irradiated atmospheres is currently unknown. Nevertheless, models used to infer thermal inversions in the literature have either used parameterized visible opacity sources (Burrows et al. 2008) or parametric temperature profiles (Madhusudhan & Seager 2009, also used in the present work). To first order, the lack of a thermal inversion in WASP-14b might indicate that the vertical mixing in the dayside atmosphere of WASP-14b is weaker compared to the downward diffusion of TiO and VO.

Spitzer has observed a number of strongly irradiated hot Jupiters with brightness temperatures in the 1000–2000 K range. The inferences of thermal inversions from emission photometry result from flux excesses in molecular bands where strong absorption is expected (Madhusudhan & Seager 2010). In principle, detection of a thermal inversion is possible with just two *Warm Spitzer* channels with sufficient S/N if there is a large flux difference between channels 1 and 2 (Knutson et al. 2008, 2009a; Madhusudhan & Seager 2010; Machalek et al. 2009; O'Donovan et al. 2010; Christiansen et al. 2010). Based on the TiO/VO hypothesis described above, Fortney et al. (2008) suggested that depending on the level of irradiation from their parent star, irradiated planets can fall into two categories: the very

Table 11
System Parameters of WASP-14

Parameter	Value	Reference
Orbital parameters		
Orbital period, P (days)	2.2437661 ± 0.0000011	a
Semimajor axis, a (AU)	0.036 ± 0.001	b
Transit time (BJD_{TDB})	$2454827.06666 \pm 0.00024$	a
Orbital eccentricity, e	0.087 ± 0.002	a
Argument of pericenter, ω (deg)	-107.1 ± 0.5	a
Velocity semiamplitude, K (m s^{-1})	990.0 ± 3	a
Center-of-mass velocity γ (m s^{-1})	-4987.9 ± 1.6	a
Stellar parameters		
Spectral type	F5V	b
Mass, M_* ($M_\odot$)	$1.211^{+0.127}_{-0.122}$	b
Radius, R_* ($R_\odot$)	$1.306^{+0.066}_{-0.073}$	b
Mean density, ρ_* ($\rho_\odot$)	$0.542^{+0.079}_{-0.060}$	b
Effective temperature, $T_{\rm eff}$ (K)	6475 ± 100	b
Surface gravity, log g_* (cgs)	$4.287^{+0.043}_{-0.038}$	b
Projected rotation rate, $v_* \sin(i)$ (km s^{-1})	4.9 ± 1.0	b
Metallicity [M/H] (dex)	0.0 ± 0.2	b
Age (Gyr)	$\sim$0.5–1.0	b
Distance (pc)	160 ± 20	b
Lithium abundance, log N(Li)	2.84 ± 0.05	b
Planetary parameters		
Transit depth, $(R_{\rm p}/R_{\rm star})^2$	$0.0102^{+0.0002}_{-0.0003}$	b
Mass, $M_{\rm p}$ ($M_{\rm J}$)	$7.341^{+0.508}_{-0.496}$	b
Radius, $R_{\rm p}$ ($R_{\rm J}$)	$1.281^{+0.075}_{-0.082}$	b
Surface gravity, log $g_{\rm p}$ (cgs)	$4.010^{+0.049}_{-0.042}$	b
Mean density, $\rho_{\rm p}$ (g cm^{-3})	4.6	b
Equilibrium temperature ($A = 0$), $T_{\rm eq}$ (K)	$1866.12^{+36.74}_{-42.09}$	b

Notes.
[a] Our analyses (see Section 6).
[b] Joshi et al. (2009).

highly irradiated atmospheres that host thermal inversions and the less-irradiated ones that do not. However, recent observations have revealed several counterexamples to this hypothesis. Machalek et al. (2008) present evidence for a temperature inversion in XO-1b, despite low irradiation of the planet ($T_{\rm eq} =$ 1209 K), while Fressin et al. (2010) show no thermal inversion, although TrES-3b is a highly irradiated planet ($T_{\rm eq} = 1643$ K). Similarly, WASP-12b, one of the most irradiated hot Jupiters known, has also been reported to lack a significant thermal inversion (Madhusudhan et al. 2011a). In this paper, we present WASP-14b as another counterexample. It is possible that additional parameters (e.g., metallicity, surface gravity, C/O ratio) influence the presence or the absence of a temperature inversion. However, more observations are needed to explain WASP-14b's missing inversion.

9. CONCLUSIONS

During two secondary eclipse events, *Spitzer* observed WASP-14b in three IRAC channels: 3.6, 4.5, and 8.0 μm. All eclipses have a high S/N (3.6 μm channel $\sim$25, 4.5 μm channel $\sim$12, 8.0 μm channel $\sim$8), which allowed us to constrain the planetary spectrum and orbital parameters.

Our observations probe the atmosphere at pressures between 0.01 and 1 bar and indicate the absence of a significant thermal inversion in the dayside atmosphere of WASP-14b. Given WASP-14b's highly irradiated atmosphere, this contradicts predictions that the most-irradiated hot Jupiters should have thermal inversions due to gaseous TiO/VO (Fortney et al. 2008). Additionally, our observations place nominal constraints on the chemical composition and day-night energy redistribution in the atmosphere of WASP-14b. We find that the data can be explained by non-inversion models with nearly solar abundances in chemical equilibrium. A factor of 10 less CO and a factor of 6 higher H_2O, compared to those obtained with solar abundances, explain the data to within the 1σ uncertainties, on average. Such CO depletion and H_2O enhancement are, in principle, possible in chemical equilibrium with C/O ratios lower than solar. More data are required to constrain the atmospheric composition of WASP-14b better.

Because the planet is much brighter than its predicted equilibrium temperature for uniform redistribution ($T_{\rm eq} = 1866$ K), the best-fitting models limit day-night energy redistribution in WASP-14b to $\leqslant$30% for zero Bond albedo. Thermal phase-curve observations can probe the nightside emission directly and better constrain this quantity.

WASP-14b is one of the most massive transiting planets known, along with CoRoT-3b (Triaud et al. 2009; Deleuil et al. 2008), HAT-P-2b (Bakos et al. 2007; Winn et al. 2007; Loeillet et al. 2008b), XO-3b (Hébrard et al. 2008; Johns-Krull et al. 2008; Winn et al. 2008), and WASP-18b (Nymeyer et al. 2011). With the exception of WASP-18b, all of these objects have very eccentric orbits. Classically, closer planets should have more

circular orbits due to greater tidal orbital decay. At distances $a < 0.1$ AU, circularization should occur in typically a few Myr, compared to common system ages of a few Gyr. However, Pont et al. (2011) argue that the time to circularize scales with the planet-star mass ratio, and is also a steep function of the orbital separation scaled to the planet radius (see their Figure 3). For planets with $M > M_J$, the mass-period relation (see their Figure 2) suggests that heavier planets get circularized very close to their parent star, or may not ever reach circularization in their lifetime. A possible explanation is that the planet raises tides on its host star strong enough that the angular momentum of the planet is transferred to the stellar spin, and the planet gets swallowed by the star. This does not oppose the classical tide theory (e.g., Goldreich & Soter 1966), but rather suggests that stopping mechanisms and tidal circularization are related. WASP-14b also has unusually high density for a hot Jupiter, similar to that of some rocky planets (4.6 g cm^{-3}). The planet's strong signal makes it ideal for further observation to constrain its composition and thus possible formation mechanisms for it and similar objects.

We thank Heather Knutson for providing the 3.6 μm *Spitzer* data prior to their public release, and Andrew Collier Cameron for useful discussions. We also thank contributors to SciPy, Matplotlib, and the Python Programming Language; other contributors to the free and open-source community; the NASA Astrophysics Data System; and the JPL Solar System Dynamics group for free software and services. This work is based on observations made with the *Spitzer Space Telescope*, which is operated by the Jet Propulsion Laboratory, California Institute of Technology under a contract with NASA. NASA provided support for this work through an award issued by JPL/Caltech and Astrophysics Data Analysis Program grant NNX13AF38G. N.M. acknowledges support from the Yale Center for Astronomy and Astrophysics through the YCAA postdoctoral Fellowship. J.B. was partially supported by NASA Earth and Space Sciences Fellowship NNX12AL83H.

Facility: Spitzer

APPENDIX

SYSTEM PARAMETERS

Table 11 lists WASP-14 system parameters derived from our analysis and the literature. The eclipse parameters are listed in Tables 7 and 8.

REFERENCES

Anderson, D. R., Hellier, C., Gillon, M., et al. 2010, ApJ, 709, 159
Anderson, D. R., Smith, A. M. S., Lanotte, A. A., et al. 2011, MNRAS, 416, 2108
Arras, P., Burkart, J., Quataert, E., & Weinberg, N. N. 2012, MNRAS, 422, 1761
Bakos, G. Á., Kovács, G., Torres, G., et al. 2007, ApJ, 670, 826
Balachandran, S. 1995, ApJ, 446, 203
Ballard, S., Charbonneau, D., Deming, D., et al. 2010, PASP, 122, 1341
Boesgaard, A. M., & Tripicco, M. J. 1986, ApJ, 303, 724
Borysow, A. 2002, A&A, 390, 779
Borysow, A., Jorgensen, U. G., & Zheng, C. 1997, A&A, 324, 185
Burrows, A., Budaj, J., & Hubeny, I. 2008, ApJ, 678, 1436
Campo, C. J., Harrington, J., Hardy, R. A., et al. 2011, ApJ, 727, 125
Castelli, F., & Kurucz, R. L. 2004, arXiv:astro-ph/0405087
Charbonneau, D., Allen, L. E., Megeath, S. T., et al. 2005, ApJ, 626, 523
Christiansen, J. L., Ballard, S., Charbonneau, D., et al. 2010, ApJ, 710, 97
Collier Cameron, A., Pollacco, D., Street, R. A., et al. 2006, MNRAS, 373, 799
Collier Cameron, A., Wilson, D. M., West, R. G., et al. 2007, MNRAS, 380, 1230
Deleuil, M., Deeg, H. J., Alonso, R., et al. 2008, A&A, 491, 889
Désert, J.-M., Lecavelier des Etangs, A., Hébrard, G., et al. 2009, ApJ, 699, 478
Eastman, J., Siverd, R., & Gaudi, B. S. 2010, PASP, 122, 935
Fazio, G. G., Hora, J. L., Allen, L. E., et al. 2004, ApJS, 154, 10
Fortney, J. J., Lodders, K., Marley, M. S., & Freedman, R. S. 2008, ApJ, 678, 1419
Fortney, J. J., Marley, M. S., & Barnes, J. W. 2007, ApJ, 659, 1661
Freedman, R. S., Marley, M. S., & Lodders, K. 2008, ApJS, 174, 504
Fressin, F., Knutson, H. A., Charbonneau, D., et al. 2010, ApJ, 711, 374
Gelman, A. 2002, in Encyclopedia of Environmetrics vol 3, ed. A. H. El-Shaarawi & W. W. Piegorsch (Chichester, NY: Wiley), 1634
Gelman, A., & Rubin, D. 1992, StaSc, 7, 457
Giménez, A., & Bastero, M. 1995, Ap&SS, 226, 99
Goldreich, P., & Soter, S. 1966, Icar, 5, 375
Harrington, J., Luszcz, S., Seager, S., Deming, D., & Richardson, L. J. 2007, Natur, 447, 691
Hébrard, G., Bouchy, F., Pont, F., et al. 2008, A&A, 488, 763
Hubeny, I., Burrows, A., & Sudarsky, D. 2003, ApJ, 594, 1011
Husnoo, N., Pont, F., Hébrard, G., et al. 2011, MNRAS, 413, 2500
Jeffreys, H. 1961, Theory of Probability (3rd ed.; Oxford: Oxford Univ. Press)
Johns-Krull, C. M., McCullough, P. R., Burke, C. J., et al. 2008, ApJ, 677, 657
Joshi, Y. C., Pollacco, D., Collier Cameron, A., et al. 2009, MNRAS, 392, 1532
Karkoschka, E., & Tomasko, M. G. 2010, Icar, 205, 674
Knutson, H. A., Charbonneau, D., Allen, L. E., Burrows, A., & Megeath, S. T. 2008, ApJ, 673, 526
Knutson, H. A., Charbonneau, D., Burrows, A., O'Donovan, F. T., & Mandushev, G. 2009a, ApJ, 691, 866
Knutson, H. A., Charbonneau, D., Cowan, N. B., et al. 2009b, ApJ, 703, 769
Knutson, H. A., Charbonneau, D., Deming, D., & Richardson, L. J. 2007, PASP, 119, 616
Knutson, H. A., Howard, A. W., & Isaacson, H. 2010, ApJ, 720, 1569
Levenberg, K. 1944, QApMa, 2, 164
Liddle, A. R. 2007, MNRAS, 377, L74
Loeillet, B., Bouchy, F., Deleuil, M., et al. 2008a, A&A, 479, 865
Loeillet, B., Shporer, A., Bouchy, F., et al. 2008b, A&A, 481, 529
Lust, N. B., Britt, D. T., Harrington, J., et al. 2013, PASP, submitted
Machalek, P., McCullough, P. R., Burke, C. J., et al. 2008, ApJ, 684, 1427
Machalek, P., McCullough, P. R., Burrows, A., et al. 2009, ApJ, 701, 514
Madhusudhan, N. 2012, ApJ, 758, 36
Madhusudhan, N., Harrington, J., Stevenson, K. B., et al. 2011a, Natur, 469, 64
Madhusudhan, N., Mousis, O., Johnson, T. V., & Lunine, J. I. 2011b, ApJ, 743, 191
Madhusudhan, N., & Seager, S. 2009, ApJ, 707, 24
Madhusudhan, N., & Seager, S. 2010, ApJ, 725, 261
Mandel, K., & Agol, E. 2002, ApJL, 580, L171
Marquardt, D. 1963, SJAM, 11, 431
Maxted, P. F. L., Anderson, D. R., Collier Cameron, A., et al. 2011, PASP, 123, 547
Morales-Calderón, M., Stauffer, J. R., Kirkpatrick, J. D., et al. 2006, ApJ, 653, 1454
Nymeyer, S., Harrington, J., Hardy, R. A., et al. 2011, ApJ, 742, 35
O'Donovan, F. T., Charbonneau, D., Harrington, J., et al. 2010, ApJ, 710, 1551
Poddaný, S., Brát, L., & Pejcha, O. 2010, NewA, 15, 297
Pollacco, D., Skillen, I., Collier Cameron, A., et al. 2006, Ap&SS, 304, 253
Pont, F., Husnoo, N., Mazeh, T., & Fabrycky, D. 2011, MNRAS, 414, 1278
Pont, F., Zucker, S., & Queloz, D. 2006, MNRAS, 373, 231
Press, W. H., Teukolsky, S. A., Vetterling, W. T., & Flannery, B. P. 1992, Numerical Recipes in FORTRAN. The Art of Scientific Computing (2nd ed.; Cambridge: Cambridge Univ. Press)
Raftery, A. E. 1995, Sociological Methodol., 25, 111
Reach, W. T., Megeath, S. T., Cohen, M., et al. 2005, PASP, 117, 978
Rothman, L. S., Jacquemart, D., Barbe, A., et al. 2005, JQSRT, 96, 139
Seager, S., & Deming, D. 2010, ARA&A, 48, 631
Sivia, D. S., & Skilling, J. 2006, Data Analysis: A Bayesian Tutorial (2nd ed.; Oxford: Oxford Univ. Press)
Spiegel, D. S., Silverio, K., & Burrows, A. 2009, ApJ, 699, 1487
Stevenson, K. B., Harrington, J., Fortney, J. J., et al. 2012a, ApJ, 754, 136
Stevenson, K. B., Harrington, J., Lust, N. B., et al. 2012b, ApJ, 755, 9
Stevenson, K. B., Harrington, J., Nymeyer, S., et al. 2010, Natur, 464, 1161
Tinetti, G., Vidal-Madjar, A., Liang, M.-C., et al. 2007, Natur, 448, 169
Triaud, A. H. M. J., Queloz, D., Bouchy, F., et al. 2009, A&A, 506, 377
Werner, M. W., Roellig, T. L., Low, F. J., et al. 2004, ApJS, 154, 1
Winn, J. N., Holman, M. J., Torres, G., et al. 2008, ApJ, 683, 1076
Winn, J. N., Johnson, J. A., Peek, K. M. G., et al. 2007, ApJL, 665, L167